Combustion Field Prediction and Diagnosis via Spatiotemporal Discrete U-ConvLSTM Model

Xiaodong Huang, Xiaojian Hao, Baowu Pan, Shaogang Chen, Shenxiang Feng, and Pan Pei

***Abstract*—Considering the importance of combustion diagnosis in industrial manufacturing and many fields, efficient, quick, and real-time multidimensional reconstruction is necessary and indispensable. Hence, focusing on the combustion field dynamic and multi-dimensional reconstruction, a modified U-ConvLSTM model was proposed to combine with the TDLAS method to resolve the real-time reconstruction and short prediction. By dividing the combustion field into space and time slices, we used discretized spatiotemporal slices to complete the 2-D distribution reconstruction and then expanded them into higher dimensions. The simulation results demonstrate that our design can effectively reconstruct different 2-D distributions, achieving a reconstruction error of less than 5%. Three-step predictions also performed well, a PSNR no less than 30 dB, and an SSIM no less than 0.75. In general, our multidimensional combustion field reconstruction method, based on the spatiotemporal discretization U-ConvLSTM model, can enhance the accuracy of combustion field reconstruction and provide short-term predictions. This work will contribute to closed-loop control in industrial fields.**

***Index Terms*—Tunable diode laser absorption spectroscopy (TDLAS), U-model convolutional long short-term memory (U-ConvLSTM), combustion site, reconstruction, predicted.**

I. Introduction

As THE environment changes everywhere, global warming accelerates [1], [2], [3], [4], [5]. How to use limited energy to meet production and living needs and control greenhouse gas emissions is crucial. Combustion is one of the most important processes in industrial production, covering energy consumption and gas emissions. Combustion diagnostics are an effective method to detect combustion performance, efficiency and emissions.

Because of the critical role of multi-parameter detection in combustion, many re-searchers have focused on typical combustion fields in industrial manufacturing and military defense. These include detection and monitoring of high-temperature boilers, combustion diagnosis of aerospace engine combustion chambers [6], and assessment of damage efficiency of high-temperature explosion fireballs. However, fire detection, monitoring, and prediction are also necessary to ensure life safety.

The distribution of the temperature field and gas concentration field can directly and effectively reflect the combustion state, providing an essential method for evaluating the combustion field. Therefore, many researchers aim to redefine combustion diagnostics as temperature and concentration field diagnostics rather than focusing solely on flames or chemical reactions.

Common temperature measurement methods can be broadly categorized into two types: contact and non-contact measurements, each applicable in different scenarios. With the advancement of new sensors and sensor techniques, particularly spectral detection methods such as absorption spectroscopy, non-contact measurement methods have gained popularity. These techniques, known for their non-invasive nature, rapid response, and high sensitivity [7], [8], are generally well-suited to meet the demands of a wide variety of complex and harsh combustion sites. To accurately represent the combustion field's distribution and analyze combustion conditions, researchers are working on reconstructing the 2-D or 3-D distributions of temperature, concentration, or pressure.

On the one hand, due to the limitations of line of sight (LOS) [9], the detected data represent the integral along the optical path. Therefore, it's necessary to utilize computed tomography (CT) techniques to reconstruct the distribution of parameters. Traditional methods, such as filtered back projection (FBP) and the algebraic reconstruction technique (ART) [10], [11], [12], [13], are used to invert the actual distribution of temperature or other parameters in the combustion field. Xu, Liu, et al. [14], [15], [16], [17] used a pentagonal TDLAS detection system and CT-TDLAS to accomplish the 2-D reconstruction of temperature and H2O concentration in swirl combustion. Choi et al. [18] deployed multi-angle temperature detection equipment that divided the combustion field into a 22 × 22 square mesh grid. Jeon et al. [19] constructed a CT-TDLAS system with 16-path cells to measure the 2-dimensional temperature distribution of a propane-air pre-mixed flame, which covered various fuel mixing conditions.

On the other hand, given the complexity of the combustion sitest, it is challenging to arrange a large number of lasers and detectors for detection, leading to data scarcity and reconstruction difficulties. Conversely, an excess of data can hinder real-time reconstruction, failing to meet the demands of dynamic combustion detection and reconstruction.

Manuscript received 12 December 2023; revised 25 January 2024; accepted 13 February 2024. Date of current version 1 March 2024. This work was supported in part by the National Natural Science Foundation of China under Grant 52075504, in part by the Fund for Shanxi 1331 Project Key Subject Construction under Grant 1331PKSC, in part by the State Key Laboratory of Quantum Optics and Quantum Optics Devices under Grant KF202301, and in part by the Shanxi Key Laboratory of Advanced Semiconductor Optoelectronic Devices and System Integration under Grant 2023SZKF11. *(Corresponding author: Xiaojian Hao.)*

The authors are with the State Key Laboratory of Dynamic Measurement Technology, North University of China, Taiyuan 030051, China, and also with the Science and Technology on Electronic Test and Measurement Laboratory, North University of China, Taiyuan 030051, China (e-mail: haoxiaojian @nuc.edu.cn).

Digital Object Identifier 10.1109/JPHOT.2024.3366425

Therefore, some researchers have tried soft measurements to realize high-quality re-construction of the region of interest (ROI). Cai et al. [20] used a deep learning method to improve the reconstruction, such as the convolutional neural network (CNN), and indicated that unsupervised or semi-supervised deep learning models such as deep belief networks (DBN) and generative adversarial networks (GAN), have a possible and better application in the tunable diode laser absorption (TDLAS) tomography reconstruction field.

The concept of spatiotemporal discretization was introduced by Klapproth et al. [21] in 2015. Since then, the rise of deep learning has led some researchers to explore this concept further. They aim to predict movement and forecast precipitation using images like radar echo maps [22], [23]. Wang et al. [24] also improved the PredRNN method to obtain good results for both action-free and action-conditioned predictive performance. Through these studies, we determined that the dynamic combustion process can also be discretized with the spatiotemporal slice; using these slices, we can realize the reconstruction under the time and spatial dimensions, which will be beneficial for the detection, diagnosis, and prediction. However, in the field of dynamic combustion, there are few reports on predicting temperature distribution.

In the article, we propose an improved U-ConvLSTM model to reconstruct and predict the multi-parameter distribution within the combustion field. Based on the TDLAS temperature detection and reconstruction method, the feasibility of a multi-parameter distribution reconstruction technology is demonstrated, and the dynamic reconstruction of the temperature distribution is achieved through spatio-temporal discretization. First, we select appropriate laser spectrum line pairs, build a TDLAS detection system to measure the combustion field, get projection data and thereby establish an optical detection model. Then, the U-ConvLSTM model is designed for subsequent reconstruction, training, prediction and performance verification of combustion field temperature distribution. Finally, we can demonstrate the superior performance of our U-ConvLSTM reconstruction and prediction method through comparison with different temperature reconstruction methods.

II. Math

A. Tunable Diode Laser Absorption Spectroscopy and Tomographic Methods

Tunable diode laser absorption spectroscopy (TDLAS) is a popular absorption spectroscopy technique [8], [9], [10], featuring a quick response and high selectivity. The mathematical background of TDLAS is the Beer–Lambert law, which is shown in Fig. 1, and the absorbance $\alpha(\nu)$ dependent on the wavenumber ν [cm^{-1}] can be defined as:

$$\alpha(\nu) = \frac{I_t(\nu)}{I_o(\nu)} = \exp\{-k_\nu L\} = \exp\{-S(T)PX\varphi(\nu,T)\cdot L\} \tag{1}$$

where $I_t(\nu)$ and $I_i(\nu)$ are the intensities of the transmitter laser and the incident laser, P [atm] is the total pressure of the region of interest, X is the concentration of the material under test,

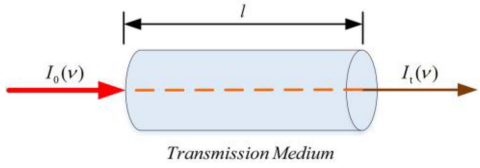

Fig. 1. Schematic diagram of Beer-Lambert law.

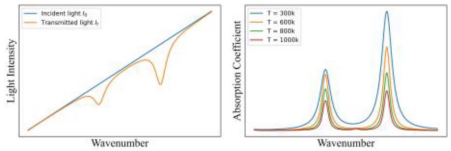

Fig. 2. Schematic diagram of TDLAS: (a) the relationship of incident light and the transmitted light with development of wavenumber; (b) the relationship of the center wavenumber and ab-sorption coefficient under different temperature.

and $S[T(x)]$ [cm^{-2}·atm^{-1}] is the line strength of the molecular transition of the absorbing species, which is dependent on the temperature [22], [23], $\varphi(\nu, T)$ [cm] is the line-shape function. The relationship between the incident light and the transmitted light is shown in Fig. 2(a), and the relationship between the absorption coefficient $\alpha(\nu)$ and wavenumber at different temperatures is shown in Fig. 2(b).

The path based integrated absorbance A_i is:

$$A_i = \int_a^b a_{\nu_i}(l)dl = \int_a^b P\cdot S_{\nu_i}[T]\cdot X\cdot\varphi(\nu,T)dl \tag{2}$$

where line strength S[T] is a function of temperature, and the relationship can be described as:

$$S(T) = S(T_0)\frac{Q(T_0)}{Q(T)}\frac{T_0}{T} \cdot \exp\left\{-\frac{hcE''_i}{k}\left(\frac{1}{T}-\frac{1}{T_0}\right)\frac{1-\exp\left(\frac{-hc\nu_{0,i}}{kT}\right)}{1-\exp\left(\frac{-hc\nu_{0,i}}{kT_0}\right)}\right\} \tag{3}$$

$Q(T_0)$ and $Q(T)$ are partition functions of gas absorption molecules at temperatures T_0 and T, which can be fitted by a third-order polynomial of temperature and can be ex-pressed as:

$$Q(T) = \mathrm{a} + bT + cT^2 + dT^3 \tag{4}$$

In addition, the HITRAN spectral database [25] online website (HITRAN on the Web) provides a large number of molecular partition function curve with temperature change, which can be queried, or directly called by Python through HAPI.

In this way, we can calculate the value of temperature T based on the two selected spectral lines as follows, where h [J·S] and c [m/s] are the Planck constant and speed of light, respectively, h [J/K] is Boltzmann constant, T_0 is defined as 296 K, A_1 and A_2 are the absorbances of different absorption lines.

$$T = \frac{\frac{hc}{k}(E_1'' - E_2'')}{\ln\left(\frac{A_1}{A_2}\right) + \ln\left(\frac{S_2(T_0)}{S_1(T_0)}\right) + \left(\frac{hc}{k}\right)\left(\frac{E_1''-E_2''}{T_0}\right)} \tag{5}$$

Meanwhile, the concentration X of the detected gas molecules shall be:

$$X = \frac{A}{PS(T)\varphi(\nu, T)L} \tag{6}$$

In practical applications, we divide the ROI into grids to simplify the calculation, and (2) can be discretized as:

$$A_i(\nu) = \sum_{m=1}^{M}\sum_{n=1}^{N} \alpha_{mn}(T_{mn}, X_{mn}, \nu) \cdot l_{mn}^{\nu} \tag{7}$$

where $m \times n$ is the distribution of the grids, k is the number of beams, and l_{mn}^{ν} is the ab-sorption path length of the k^{th} laser beam through the pixel (m, n). It can be expressed in matrix form in (8).

An absorption path isn't comprised solely of one parameter's information about the combustion field. Consequently, when we select different types of absorption lines, we can simultaneously reconstruct multiple parameters. This technique is referred to as Nonlinear Tomographic Absorption Spectroscopy (NTAS) [21] in some studies, which uses known projection data to infer the spatial distribution of the entire field, and can use regularization techniques and optimization algorithms to improve reconstruction the difference between the value and the actual measured value.

$$A_{\nu_i} = F \cdot \alpha_{\nu_i},$$

$$F = \begin{bmatrix} f_{1,1} & f_{1,2} & \cdots & f_{1,n-1} & f_{1,n} \\ f_{2,1} & f_{2,2} & \cdots & f_{2,n-1} & f_{2,n} \\ \vdots & \vdots & & \vdots & \vdots \\ f_{m-1,1} & f_{m-1,2} & \cdots & f_{m-1,n-1} & f_{m-1,n} \\ f_{m,1} & f_{m,2} & \cdots & f_{m,n-1} & f_{m,n} \end{bmatrix}$$

$$\left(f_{mn} = \begin{cases} 0, (l \cap mn = \emptyset) \\ l_{mn}, (l \cap mn \neq \emptyset) \end{cases} \right),$$

$$\begin{bmatrix} \alpha_{1,1} \ldots \alpha_{1,n} \\ \vdots \ \ddots \ \vdots \\ \alpha_{m,1} \ldots \alpha_{m,n} \end{bmatrix}_{\nu_1}, \begin{bmatrix} \alpha_{1,1} \ldots \alpha_{1,n} \\ \vdots \ \ddots \ \vdots \\ \alpha_{m,1} \ldots \alpha_{m,n} \end{bmatrix}_{\nu_2} \cdots \begin{bmatrix} \alpha_{1,1} \ldots \alpha_{1,n} \\ \vdots \ \ddots \ \vdots \\ \alpha_{m,1} \ldots \alpha_{m,n} \end{bmatrix}_{\nu_i} \tag{8}$$

Similarly, 2-D detection and reconstruction can be described as shown in Fig. 3. X and Y make up the meshing grid of the 2-D distribution, and each grid is on behalf the absorbance of this place, which is dependent on the wavenumber and is shown with dimension Z. By computing the 3-D tensor, we realize the multi-parameter distribution reconstruction.

B. Deep Convolutional Neural Networks

The 2-D reconstruction of the combustion field can be transformed into an image generation problem for extracting, generating, and predicting image features. Therefore, the key can be considered as how to extract and learn from image features, including color, texture, shape, and local feature points. Among these, local features exhibit good stability and are not easily influenced by the external environment.

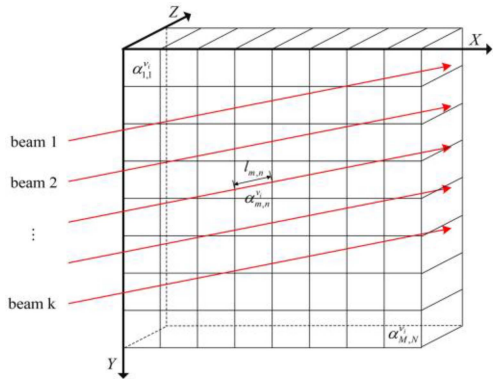

Fig. 3. Transforming 2-D parameter distribution into 3-D tensor based on the TDLAS combustion diagnosis method.

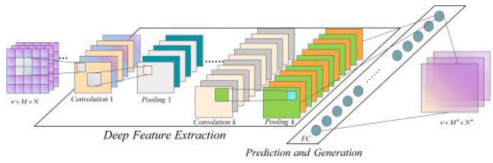

Fig. 4. Schematic diagram of the typical structure of deep convolutional neural network for prediction and generation.

Deep Convolutional Neural Networks (DCCNs) have proven effective in addressing the problem of image feature extraction, which benefits from their local receptive fields, shared weights, and pooling. A typical DCCN includes multiple sets of convolutional layers, pooling layers, and non-linear activation functions. The convolutional layer is used to extract spatial information represented in images, while the pooling layer is used to re-duce the spatial size and prevent overfitting. This way, it can decrease the amount of data processing while retaining useful information, fulfilling the need for rapid computation. Through multiple convolutional layers, discriminative local image features can be de-scribed and extracted, which play a significant role in subsequent generation.

The typical model of DCCN is shown in Fig. 4 and the whole process can be de-scribed:

a) Design and select the convolutional and pooling layers, including the kernel size, number, and connection, with the aim of extracting the deep features of the input projection data.
b) By driving the feature maps into a one-dimensional feature vector with a full connection, we can then multiple the coefficient matrix and add the biases on the vector to the vector and generate the predicted distribution.
c) Calculate the loss function, set a reasonable learning rate, decrease the loss, and optimize the model.
d) Deploy and invoke the optimal model.

In our design, the DCNN model was used to generate and predict a distribution, so the loss function we used was the mean squared error (MSE), defined as:

$$loss_{MSE} = \frac{1}{n}\sum_{i=1}^{n}(y_i^* - y_i)^2 \tag{9}$$

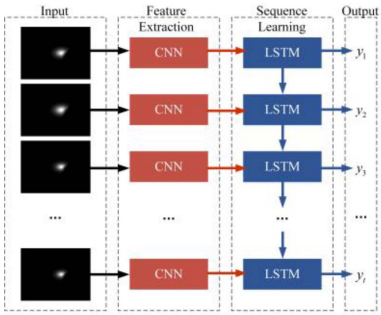

Fig. 5. Schematic diagram of ConvLSTM spatiotemporal discretization reconstructive method based on the combustion field.

where n is the size of the output of the model, y^* and y are the true value and the generated value (predicted value) of the output. By repeating training and optimizing the model, decreasing the loss function value, the structure parameters are determined and ready to be used for the generation and prediction.

C. Spatiotemporal Long Short-Term Memory

The combustion field is a dynamic and continuous process, which is difficult to calculate, and must be discretized. Inside every cell in the $m \times n$ discretized grid, several measurements are determined by ν, varying over time. Therefore, the observation at any time can be represented by a tensor like $\chi \in R^{v \times m \times n}$, sharing the same structure as in Fig. 3, where R denotes the domain of the observed features. By recording the observations peri-odically, we obtained a sequence of tensors $\hat{\chi}_1, \hat{\chi}_2, \cdots, \hat{\chi}_t$.

The spatiotemporal sequence forecasting problem is to predict the most likely length-K sequence in the future, given previous J observations that include the current one [18].

$$\begin{aligned} &\hat{\chi}_{t+1}, \hat{\chi}_{t+2}, \cdots, \hat{\chi}_{t+K} \\ &= \underset{\hat{\chi}_{t+1}, \hat{\chi}_{t+2}, \cdots, \hat{\chi}_{t+K}}{\arg\max} \\ &\quad \times p\left(\chi_{t+1,}, \cdots, \chi_{t+K} | \hat{\chi}_{t-J+1}, \hat{\chi}_{t-J+2}, \cdots, \hat{\chi}_t\right) \end{aligned} \quad (10)$$

To forecast the combustion field multi-parameter, the observation at each timestamp is the 2-D distribution feature map when we are forced on just one parameter, such as the temperature 2-D distribution.

Long short-term memory (LSTM) is a type of RNN, which has shown a good effect in the time prediction process, such as aero-engine remaining useful life prediction [26], [27]. However, when it comes to image prediction, LTSM has a weak effect on the spatial correlation.

The integration of Convolutional Neural Networks (CNNs) and Conv-LSTM [22] is pivotal in extracting image features. This is especially true for predicting and generating spatiotemporal discrete fields. For example, Fig. 5 shows the discretized combustion temperature distribution divided into spatiotemporal slices. These slices are dependent on dynamic time and display spatial distribution information. Initially, distribution images are fed into the CNN model. This model extracts feature information, which includes both the statistical 2-D distribution and dynamic changing rules. The extracted feature maps, now in vector form, are inputted into the LSTM. This process is designed to capture temporal relations. In this two-step approach, the focus of the first step is primarily on spatial information. The second step, in contrast, concentrates on temporal information.

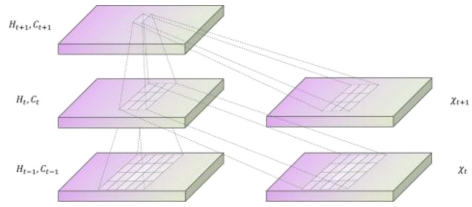

Fig. 6. Typical Structure of LSTM.

The principle of the LSTM is described in (10) and shown in Fig. 6. The key process of the LSTM is how to handle the new input, the status to be forgotten, and save the useful data, covering the three different gates.

(χ_t : input at time t; W : weight; $\circ$: Hadamard product).

a) Input process: If the input gate i_t is activated, the information will be accumulated in the cell.

b) Forget process: if the forget gate f_t is on, the past cell status c_{t-1} could be "forgotten".

c) Save process: whether the latest cell output c_t will be propagated to the final state h_t is further controlled by the output gate o_t.

$$\begin{aligned} i_t &= \sigma(W_{xi} * \chi_t + W_{hi} * \mathrm{H}_{t-1} + W_{ci} \circ c_{t-1} + b_i) \\ f_t &= \sigma(W_{xf} * \chi_t + W_{hf} * \mathrm{H}_{t-1} + W_{cf} \circ c_{t-1} + b_f) \\ c_t &= f_t \circ c_{t-1} + i_t \circ \tanh\left(W_{xc} * \chi_t + W_{hc} * \mathrm{H}_{t-1} + b_f\right) \\ o_t &= \sigma\left(W_{xo} * \chi_t + W_{ho} * \mathrm{H}_{t-1} + W_{co} \circ c_t + b_o\right) \\ \mathrm{H}_t &= o_t \circ \tanh(c_t) \end{aligned} \quad (11)$$

More complex structures can be formed if more layers can be stacked and temporally concatenated, meeting different environmental needs, and can be applied to solve many real-life spatiotemporal prediction problems.

The above describes the working principles of TDLAS and ConvLSTM. The function of TDLAS is to detect the optical projection information of the temperature in the combustion field, which is used as the input of the subsequent prediction model. The role of ConvLSTM is to extract image features. As the third step of the prediction model, it will solve the problem of prediction and generation of spatiotemporal discrete fields.

III. Implementation of the Reconstruction Method

A. Simplified Mathematical Model

With the aim of making our designed combustion field multi-dimensional reconstructive method based on spatiotemporal discretization easier to understand, we have analyzed the mathematical model of the entire system.

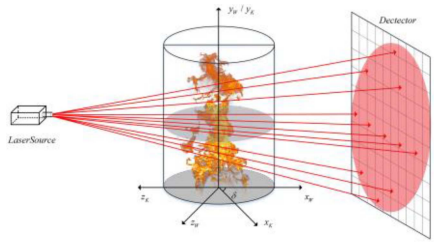

Fig. 7. Schematic diagram of combustion field diagnosis based on TDLAS photoelectric detection system.

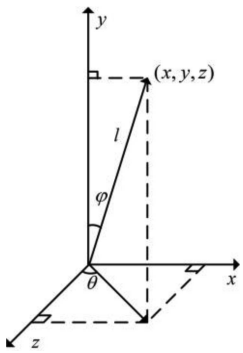

Fig. 8. Schematic diagram of conversion between cartesian coordinates and polar coordinates.

A schematic of the TDLAS combustion field detection system is shown in Fig. 7. From left to right are the DFB laser controller, the combustion field, often called the region-of-interest (ROI) and the photoelectric detection device. With the aim of saving the equipment input, we take advantage of a lens to change the collimation laser to cone-beam and realize the 3-dimensional field measurement detection, which will make a 2-dimensional surface projection on the detector. We have made only one angle projection process in Fig. 7, where (x_k, y_k, z_k) is the 3-dimensional combustion field coordinate and $(x_\omega, y_\omega, z_\omega)$ is the photoelectric detection and projection coordinate.

Through the conversion between Cartesian and polar coordinates, we can calculate the spatial coordinates of the points on the cone beam in the ROI. The conversion process is shown in Fig. 8. In this way, we can drive the body measurement into surface measurement, which means we only care for one slice of the body.

$$\begin{cases} x = l \cdot \sin\varphi \cdot \sin\theta \\ y = l \cdot \cos\varphi \\ z = l \cdot \sin\varphi \cdot \cos\theta \end{cases} \tag{12}$$

Hence, we only need to take the 2-D surface detection and reconstruction, which is shown in Fig. 9, which is one of the detection angles. In this design, we coupled the three types of lasers and took advantage of the lens to drive it into a cone beam (shown as a fan shape in 2-D). Through multi-angle detection and nonlinear computing reconstruction, the parameter distribution information is obtained.

Focusing on the slice measurement and the features of TDLAS, the nonlinear tomography reconstruction from 1-D LOS

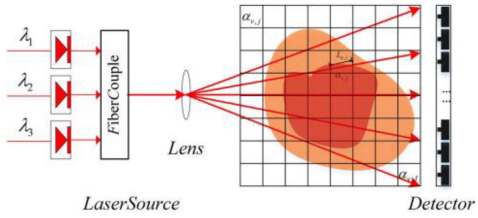

Fig. 9. One measurement slice of ROI.

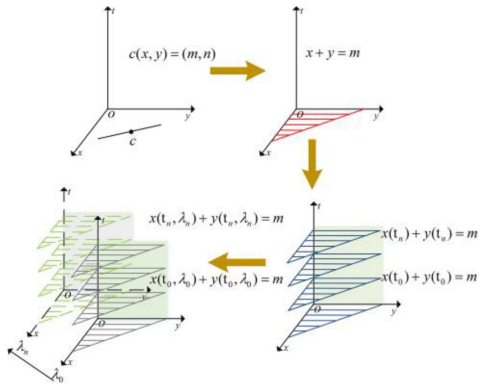

Fig. 10. Schematic diagram of nonlinear reconstruction from 1-D LOS to multi-dimension measurement.

to multi-dimensional measurement can be described as shown in Fig. 10.

B. Design of the U-ConvLSTM Model Based on Spatiotemporal Discretization and Implementation of the Reconstruction Method

The core of our method was the design and realization of the U-ConvLSTM model, which was used to generate the multiparameter distribution in the combustion field from two dimensions to multiple dimensions. The design of the model can be divided into two parts: 2-dimension distribution reconstruction and spatiotemporal discretization sequence generation and prediction.

The first step in our research involves dataset preparation. Real distribution data is hard to obtain and verify, posing challenges for proving the training and testing efficiency of our method. To tackle this, we used COMSOL, a commercial physical field simulation software. With COMSOL, we generated simulated combustion fields that featured different modal fields. These included one to three burning centers and random mixed burning peaks, as shown in Fig. 11. From these combustion simulations, we collected transient temperature distribution data of specific slices at 0.05-second intervals. To simplify computations, we applied pooling operations on the original distributions. This process resulted in 200000 distributions with a reduced resolution of 64×64. These distributions maintained an inherent spatiotemporal connection. We arranged them into sequences of 20 and randomly shuffled these 10000 groups of discrete temperature simulation sequences. We then divided these sequences into three subsets: 6000 for training, 2000 for validation, and 2000 for testing. Our main objective was to learn how to generate a 2-D distribution from projection data obtained at

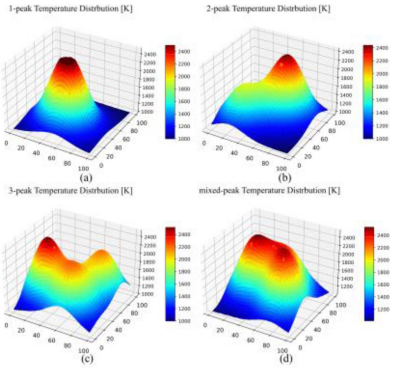

Fig. 11. Different models of temperature distribution of the simulation combustion field. (a) 1-peak temperature distribution; (b) 2-peak temperature distribution; (c) 3-peak temperature distribution; (d) mixed-peak temperature distribution.

various angles from the detector. In addressing the complexities of traditional reconstruction methods in intricate combustion sites, we considered several factors. These include the structure of the distribution, feature extraction methods, and the size of the data.

The features of the combustion field distribution are as followed:

a) In contrast to automatic driving and other image recognition fields, the distribution of the combustion field is simpler and the structure is always fixed, meaning that the image information is relatively small and all of the features are all important.
b) Compared with some complex images, the distribution of the combustion field had fewer parameters to describe. improving the risk of overfitting if we use large models such as DeepLabv3+ or SOTA.
c) In real industrial production, it was difficult to obtain a large amount of distribution data, causing the model training to drop into small sample over-fitting or un-der-fitting of the target task.

To overcome the several problems and meet the combustion field reconstruction requirements, we chose the U-Net [24]. as the base model of a deep convolutional neural network, with these three advantages:

a) Taking the low-level and high-level distribution features into consideration with the skip connection structure,
b) Maximum use limited supervisory information and a priori knowledge to design and improve the model.
c) Take the splice of feature maps, making up for the loss of edge information when we use the convolution, which cannot be recovered by deconvolution.
d) Light-weight and easy to transplant to other projects and different dynamic combustion modal needs.

In our design, we used the modified U-DCCN to realize a 2-D distribution reconstruction. The uniqueness of the U shape greatly extracts the deep feature, capture contextual, and location information, which benefits from the skip connection structure or splicing of feature maps. The deeper the network layer, the larger is the field of vision. The shallow convolution focuses on texture features, whereas the deep network focuses on the essential features.

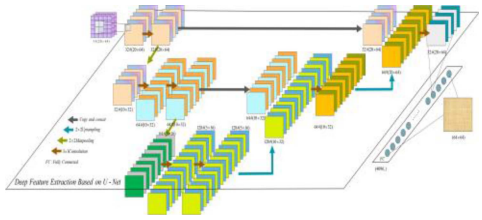

Fig. 12. Schematic diagram of the U-DCNN model structure for the 2-D distribution generation.

The input to the network consists of the detected projection data. In the initial design and development phase, we used generated simulation temperature distributions to vali-date the model and algorithm. The temperature distribution had dimensions of (64, 64), and the virtual laser projection setup included three center wavenumbers, 20 projection angles, and 64 detectors on one side. The laser path followed a fan-like pattern, as shown in Fig. 9. Therefore, the input size of the model was 3# (20, 64), where 3# represents the three types of center wavenumbers. The model architecture, as depicted in Fig. 12, can be divided into two parts: the encoder and the decoder. The encoder comprises two max-pooling layers with a kernel size of (2×2) and five convolutional layers with a kernel size of (3×3). Its primary function is to extract deep features from the input data. On the other side of the model, we have the decoder, responsible for upsampling and feature fusion. It consists of two upsampling layers (deconvolution layers) with a kernel size of (2×2) and two convolutional layers with a kernel size of (3×3). The upsampling layers in-crease the size of the feature map, while the key process involves copy and concatenation operations. Copying and concatenating allows us to preserve information lost during the max-pooling process, such as edge features that can be recovered through deconvolution. The skip connection structure enables us to fuse features from different layers, leveraging the strengths of shallow layers in capturing texture and morphology features and deep layers in capturing essential characteristics, such as the temperature distribution. This approach ensures that both low-level and high-level features are retained and well-suited for the reconstruction of the combustion field.

According to the dimensions of the projections and the shape of the temperature (T) distribution, the design of the U-DCCN architecture is shown in Fig. 12, where after the full connection layer, the feature vector is put into the spatiotemporal discretization ConvLSTM model.

The second part of our design addresses the issue of temporal correlation. Unlike most 3D reconstruction methods for the combustion field, which are time-consuming and computationally intensive, we adopted a multiple slice reconstruction approach for 3D combustion reconstruction, as illustrated in Figs. 7 and 9. By focusing on one slice of the field, we were able to rapidly reconstruct the parameter distribution. Using multiple models to process all the slices, we achieved parallel and efficient 3D field reconstruction. Additionally, since combustion is a dynamic process, it is crucial to consider the temporal relationship, which

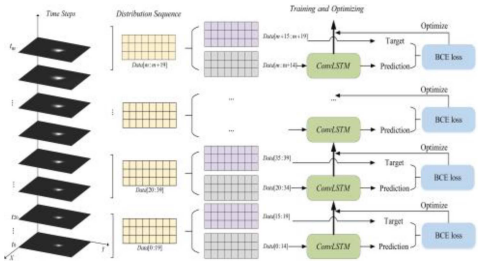

Fig. 13. Schematic diagram of the U-ConvLSTM model structure based on spatiotemporal discretization distribution sequence.

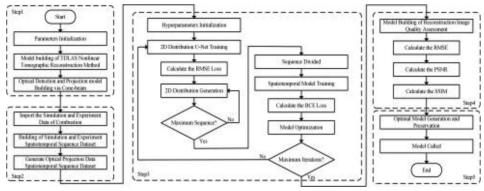

Fig. 14. Flow chart of the combustion field multi-dimensional reconstructive method via spatiotemporal discretization U-ConvLSTM model.

reflects the laws of combustion and is often overlooked in reconstruction methods.

To tackle this, we designed the U-ConvLSTM model to address these challenges. In our design, the ConvLSTM serves as a connection to learn the relationships among the spatiotemporal discretization slices. The entire system can be visualized as shown in Fig. 13.

From the global angle, the input of the model was continuous projection sequences, and each sequence consisted of 20 projection distribution slice data. We divided the sequence into two parts: the first 15 data [0:14] shall be put into the U-ConvLSTM model to train, calculate the loss, and optimize the model and generate the prediction value of the model, and the last five data points [15:19] were considered as the target output of the model. The objective function can be expressed as (12), and the aim is to generate and predict the distribution of the combustion:

$$\begin{aligned}&\hat{\chi}_{t+1}, \hat{\chi}_{t+2}, \cdots, \hat{\chi}_{t+5}\\ &= \underset{\hat{\chi}_{t+1}, \hat{\chi}_{t+2}, \cdots, \hat{\chi}_{t+5}}{\arg\max} p\left(\chi_{t+1,}, \cdots, \chi_{t+5} | \hat{\chi}_{t-14}, \hat{\chi}_{t-13}, \cdots, \hat{\chi}_{t}\right)\\ &= g_{forecasting}\left(f_{encoding}\left(\hat{\chi}_{t-14}, \hat{\chi}_{t-13}, \cdots, \hat{\chi}_{t}\right)\right)\end{aligned} \tag{13}$$

where $f_{encoding}$ was used to encode the former 15 data to search the inner link of the distribution slices and $g_{forecasting}$ was used to generate the following distribution status.

The loss function we chose to identify and optimize the prediction process was:

$$loss_{BCE}\left(x_i, y_i\right) = -w_i\left[y_i \log x_i + (1 - y_i) \log(1 - x_i)\right] \tag{14}$$

which was primarily used to create a standard for measuring the binary cross entropy between the target and output. Thus, the total loss can be described as:

$$loss = \lambda loss_{MSE} + (1 - \lambda) loss_{BCE} \tag{15}$$

In general, the U-ConvLSTM reconstruction method designed in this study has the following characteristics:

a) Modular design. We divided the different function parts into different models and designed them as shown in Fig. 14. Each part of the reconstruction method can be implemented independently, which is easier to train and transplant.

b) Lightweight small networks the total model of our design was 51.36 MB, which could be used on the embedded terminal equipment, with the aim of realizing distributed and real-time reconstruction.

C. The Quality Assessment Standard

To estimate the quality of the combustion field reconstruction, we chose three main indexes to assess the temperature distribution reconstruction image, including the root mean squared error (RMSE), peak signal-to-noise ratio (PSNR), and structural similarity (SSIM).

Combustion field reconstruction can be seen as a regression process, which means training and generating a new distribution to increasingly approach the original image, and the main evaluation criterion is the MSE or the RMSE. They can be defined as:

$$MSE = \frac{1}{mn} \sum_{i=0}^{m-1} \sum_{j=0}^{n-1} [I(i,j) - K(i,j)]^2 \tag{16}$$

$$RMSE = \sqrt{MSE} \tag{17}$$

PSNR is one of the most widely used objective measurements of image quality, which can be calculated using the MSE.

$$PSNR = 10 \cdot \log_{10}\left(\frac{MAX_I^2}{MSE}\right) = 20 \cdot \log_{10}\left(\frac{MAX_I}{\sqrt{MSE}}\right) \tag{18}$$

where $MAX = 2^n - 1$, n is the number of bits of one pixel. The higher the PSNR value, the less distortion it represents.

SSIM is a measure of the similarity between two images, x and y. It can be defined as:

$$SSIM(x,y) = \frac{(2\mu_x\mu_y + c_1) \cdot (2\sigma_{xy} + c_2)}{\left(\mu_x^2 + \mu_y^2 + c_1\right) \cdot \left(\sigma_x^2 + \mu_y^2 + c_2\right)} \tag{19}$$

where μ_x and μ_y are the averages of the two images x and y, σ_x^2, σ_y^2 is the variance of x, y. Constant c_1 and c_2 are used to maintain the stability of (11), and can be de-scribed as:

$$c_i = (k_i L)^2 (i = 1, 2) \tag{20}$$

where $k_1 = 0.01$, $k_2 = 0.03$ and L is the dynamic range of pixel values, defined as $L = 255$ in our study. The closer the SSIM value is to 1, the more similar are the two images.

IV. Results and Discussion

Our designed multi-dimensional reconstruction method mainly consists of a 2-D slice and spatiotemporal discretization multi-D combustion field reconstruction, and the accuracy and result are largely dependent on the parameters of the two neural

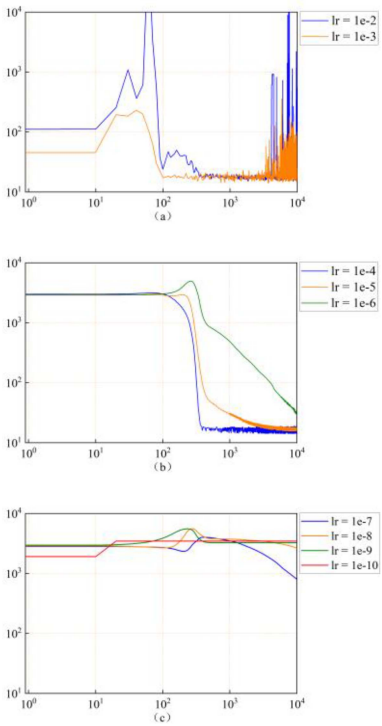

Fig. 15. Evolution of the loss function for each of the 9-learning rate; (a) excessive learning rate; (b) suitable learning rate; (c) low learning rate.

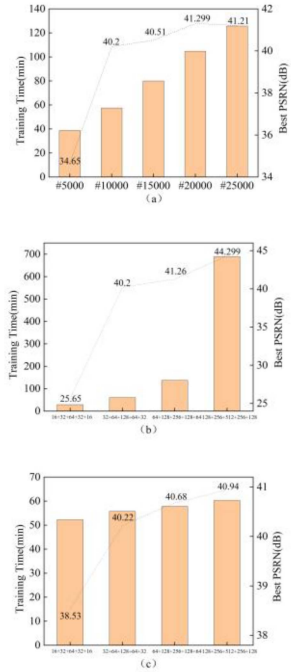

Fig. 16. The relationship between calculation time consumption, optimal PSNR and hyperparameters: (a) the number of the training samples; (b) the design of the convolution kernels; (c) the number of the latent layers.

networks, such as the learning rate l_r, the design of the convolution kernels N_k that determine the features to be extracted, and the number of the latent layer N_l that determines the prediction accuracy and the number of training samples N_s.

Hence, in this section, we focus on these parameters to determine how they affect our reconstruction results and how they should be determined to optimize our network structure. The designed method was then compared to the other two reconstruction methods.

A. *Determination of Learning Rate*

The choice of learning rate plays a significant role in network training. As shown in Fig. 15, a proper learning rate will show a good performance on the results, while on the other hand, a low learning rate will make it difficult to converge and cost a large amount of computing source, and a large learning rate can converge in a short but it is difficult to train and control.

B. *Influences of the Number of Training Samples, Latent Layers, and the Design of the Convolution Kernels*

Deep learning models are data-driven, and a sufficient number of samples should be used to extract the features during the learning process [29].

As shown in Fig. 16, by separately changing the three aspects, comparing the training time and the optimal PSNR of the results, we find that:

a) An adequate sample size is the foundation for high-quality learning. When the number was less than 10000, the model could not learn the inner relation. However, when the number was more than 10000, the accuracy did not show obvious improvement, which meant that 10000 samples could provide enough features for our mode, and more samples had too much computing time.
b) The design of convolution kernels had a greater impact on the results, determining the number of kernels or the number of deep features. Our target was 64×64, and the suit-able design was $32 + 64 + 128 + 64 + 32$, with more kernels causing high computing cost and low affect.
c) The number of latent layers did not have much influence on the results of training time and optimal PSNR, and we chose five layers in this design.

C. *Comparison With the Different Reconstruction Methods*

After determining the learning rate, number of convolution kernels, latent layers, and number of training samples, the novel U-ConvLSTM model for the reconstruction of the temperature distribution was designed with l_r = 1e-5, $N_k = 32 + 64 + 128 + 64 + 32$, $N_l = 5$, and $N_s = 10000$. To demonstrate the good performance of our proposed model, we compared it with the classic SART algorithm optimized through NSGA-III and a simple CNN model, and compare it with our method.

The results are shown in Fig. 17. It can be found that as the number of peaks increases, the reconstruction error also increases. The U-ConvLSTM model proposed in this article has good reconstruction performance, with a maximum relative error of only 4.2%, while the maximum reconstruction error of the CNN model is 8.6%, the SART maximum reconstruction error of the model is 7.4%. Simple CNN models perform poorly in

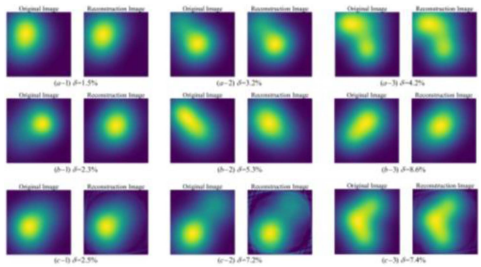

Fig. 17. Comparison of the three reconstruction methods results based on the two-dimensional temperature distribution, which was one slice of the spatiotemporal discretization combustion field. (a) Showcases the results obtained from our proposed U-ConvLSTM reconstruction method. (b) Displays the results obtained from a CNN-based computational re-construction method. (c) Exhibits the results obtained from the NSGA-III optimized SART technique. The numbers (1)–(3) represent different distribution patterns, specifically single-peak, double-peak, and triple-peak distributions, respectively.

TABLE I
THIS IS A SAMPLE OF A TABLE TITLE

Group	Prior Steps	Prediction Step	PSNR (dB)	SSIM
1	5	1	39.237	0.996
		2	33.576	0.831
		3	30.020	0.752
		4	10.432	0.269
		5	4.532	0.178
2	10	1	40.212	0.997
		2	36.552	0.842
		3	30.438	0.758
		4	10.244	0.320
		5	5.138	0.211
3	15	1	40.138	0.996
		2	36.458	0.872
		3	30.835	0.859
		4	11.828	0.335
		5	6.825	0.238
4	20	1	40.230	0.997
		2	36.252	0.891
		3	30.251	0.782
		4	12.125	0.220
		5	6.124	0.211
5	25	1	40.228	0.996
		2	36.125	0.889
		3	31.259	0.773
		4	12.222	0.229
		5	6.012	0.210

multimodal reconstruction, and SART performs poorly due to the influence of CT artifacts.

D. Results of the Different Preprocessing Steps and Prediction Steps

To compare the results of different prediction steps, we conducted tests using five sets of spatiotemporal discretization temperature distribution sequence data. Each sequence data comprised 10 to 30 distribution slices, with a time interval of 0.05s. In these tests, the previous slice data were utilized as the prior step, while the remaining data were employed for the prediction step. The complete results of these tests are presented in Table I.

It can be concluded from Table I that the first, second and third results can better predict the temperature distribution information. Their PSNR is greater than 30 dB and SSIM is greater than 0.75. However, as the number of predictions increases, the accuracy of the predictions decreases. It also decreases, their overall PSNR values are less than 13 dB, and their SSIM values are less than 0.35. It is worth noting that more prior steps will improve the prediction accuracy, but when the prior steps reaches 25, the total performance is basically the same as 20 prior steps, which means using too many distributions as prior knowledge, the model will be overfitted and degraded. Therefore, considering the computational and time costs, we combine the 20 distributions into a sequence and predict the short-term results for 3 time steps.

Predicting long-term outcomes still poses many challenges. It is crucial to consider additional combustion evolution rules and effectively incorporate them into the reconstruction or prediction process. This requires further algorithm development and careful handling of prior knowledge. By addressing these challenges, we can enhance the accuracy and reliability of predictions in the temporal dimension.

V. CONCLUSION

This paper proposes a multi-dimensional reconstruction method of combustion fields based on spatio-temporal discretization, implemented through the improved U-ConvLSTM model, aiming to solve the problem of rapid multi-dimensional reconstruction and prediction of combustion fields. According to the simulation experiment results of this study, we can find that compared with the existing simple CNN model and the NSGA-III algorithm optimized simultaneous algebraic reconstruction technology (SART), the designed U-ConvLSTM model shows better reconstruction performance and Lower time cost, and considers the time dimension to learn the inter-temporal correlation of combustion, expands the reconstruction dimension, realizes slice distribution reconstruction and short-term prediction, is more suitable for dynamic combustion processes, and quickly reconstructs and predicts temperature field distribution has good application prospects. In future research, we will try some semi-supervised or unsupervised learning methods to modify our models and methods, such as generative adversarial networks (GAN) and graph neural networks (GNN), to extract latent information from spatial and temporal data. The effectiveness of the features improves the accuracy of temperature distribution prediction in the combustion field.

Disclosures: The authors declare no conflicts of interest.

Data Availability: The data underlying the results presented in this paper are not publicly available at this time but may be obtained from the authors upon reasonable request.

ACKNOWLEDGMENT

The authors would like to thank all reviewers, editors, and contributors for their contributions and suggestions, as well as all members of the OSEC Laboratory.

REFERENCES

[1] O. Isinkaralar, "Discovery of spatial climate parameters and bioclimatic comfort change simulation in Türkiye under socioeconomic pathway scenarios: A basin-scale case study for urban environments," *Natural Hazards*, vol. 120, pp. 1809–1819, 2024.

[2] O. Isinkaralar, K. Isinkaralar, and D. Yilmaz, "Climate-related spatial reduction risk of agricultural lands on the Mediterranean coast in Türkiye and scenario-based modelling of urban growth," *Environ., Develop. Sustainability*, vol. 25, no. 11, pp. 13199–13217, 2023.

[3] O. Isinkaralar, "Spatio-temporal patterns of climate parameter changes in Western Mediterranean basin of Türkiye and implications for urban planning," *Air Qual., Atmos. Health*, vol. 16, no. 11, pp. 2351–2363, 2023.

[4] O. Isinkaralar and K. Isinkaralar, "Projection of bioclimatic patterns via CMIP6 in the Southeast Region of Türkiye: A guidance for adaptation strategies for climate policy," *Environ. Monit. Assessment*, vol. 195, no. 12, 2023, Art. no. 1448.

[5] O. Isinkaralar, "A climate-sensitive approach for determining the urban growth boundaries: Towards a spatial exploration for Bursa, Türkiye," *J. Urban Plan. Develop.*, vol. 149, no. 4, 2023, Art. no. 04023046.

[6] A. Sarmiento et al., "Raman spectroscopy as a tool to diagnose the impacts of combustion and greenhouse acid gases on properties of Built Heritage," *J. Raman Spectrosc., An International Journal for Original Work in all Aspects of Raman Spectroscopy, Including Higher Order Processes, and also Brillouin and Rayleigh Scattering*, vol. 39, no. 8, pp. 1042–1049, 2008.

[7] H. N. Yang et al., "Leakage detection of closed vials based on two-line water-vapor TDLAS," *Measurement*, vol. 135, pp. 413–417, 2019.

[8] Z. Wang et al., "Application of 2D temperature measurement to a coal-fired furnace using CT-TDLAS," *Meas. Sci. Technol.*, vol. 31, no. 3, 2019, Art. no. 035203.

[9] G. R. Cho and D. W. Choi, "Measurement enhancement of TDLAS based on variable weighted cross-correlation tomography for the simultaneous reconstruction of 2D temperature and concentration," *J. Mech. Sci. Technol.*, vol. 35, pp. 525–534, 2021.

[10] F. Wang et al., "Simultaneous measurement of 2-dimensional H_2O concentration and temperature distribution in premixed methane/air flame using TDLAS-based tomography technology," *Opt. Commun.*, vol. 346, pp. 53–63, 2015.

[11] Y. Kim et al., "Deep learning–based denoising algorithm in comparison to iterative reconstruction and filtered back projection: A 12-reader phantom study," *Eur. Radiol.*, vol. 31, no. 11, pp. 8755–8764, 2021.

[12] M. G. Jeon et al., "Evaluation of 3D measurement using CT-TDLAS," *Modern Phys. Lett. B*, vol. 33, no. 14n15, 2019, Art. no. 1940018.

[13] D. W. Choi et al., "Performance improvements in temperature reconstructions of 2-D tunable diode laser absorption spectroscopy (TDLAS)," *J. Thermal Sci.*, vol. 25, pp. 84–89, 2016.

[14] C. Liu, S.-A. Tsekenis, N. Polydorides, and H. McCann, "Toward customized spatial resolution in TDLAS tomography," *IEEE Sensors J.*, vol. 19, no. 5, pp. 1748–1755, Mar. 2019.

[15] C. Liu and L. Xu, "Laser absorption spectroscopy for combustion diagnosis in reactive flows: A review," *Appl. Spectrosc. Rev.*, vol. 54, no. 1, pp. 1–44, 2019.

[16] C. Liu, Z. Cao, Y. Lin, L. Xu, and H. McCann, "Online cross-sectional monitoring of a swirling flame using TDLAS tomography," *IEEE Trans. Instrum. Meas.*, vol. 67, no. 6, pp. 1338–1348, Jun. 2018.

[17] A. Huang, Z. Cao, W. Zhao, H. Zhang, and L. Xu, "Frequency-division multiplexing and main peak scanning WMS method for TDLAS tomography in flame monitoring," *IEEE Trans. Instrum. Meas.*, vol. 69, no. 11, pp. 9087–9096, Nov. 2020.

[18] D. W. Choi, D. H. Doh, and M. G. Jeon, "The development of the simultaneous reconstruction of 2D temperature and concentration using a 6-peaks algorithm for CT-TDLAS," *J. Mech. Sci. Technol.*, vol. 34, pp. 2067–2074, 2020.

[19] M. G. Jeon et al., "A study on two-dimensional temperature and concentration distribution of Propane-Air premixed flame using CT-TDLAS," *Modern Phys. Lett. B*, vol. 34, no. 07n09, 2020, Art. no. 2040020.

[20] J. Huang et al., "Reconstruction for limited-data nonlinear tomographic absorption spectroscopy via deep learning," *J. Quantitative Spectrosc. Radiative Transfer*, vol. 218, pp. 187–193, 2018.

[21] C. Klapproth, "The contact-stabilized Newmark method: Consistency error of a spatiotemporal discretization," *Numerische Mathematik*, vol. 131, no. 1, pp. 59–82, 2015.

[22] X. Shi et al., "Convolutional LSTM network: A machine learning approach for precipitation nowcasting," in *Proc.28th Int. Conf. Neural Inf. Process. Syst.*, 2015, pp. 802–810.

[23] X. Zhou, J. Feng, and Y. Li, "Non-intrusive load decomposition based on CNN–LSTM hybrid deep learning model," *Energy Rep.*, vol. 7, pp. 5762–5771, 2021.

[24] Y. Wang et al., "Predrnn: A recurrent neural network for spatiotemporal predictive learning," *IEEE Trans. Pattern Anal. Mach. Intell.*, vol. 45, no. 2, pp. 2208–2225, Feb. 2023.

[25] I. E. Gordon et al., "The HITRAN2020 molecular spectroscopic database," *J. Quantitative Spectrosc. Radiative Transfer*, vol. 277, 2022, Art. no. 107949.

[26] S. Xiang et al., "Multicellular LSTM-based deep learning model for aero-engine remaining useful life prediction," *Rel. Eng. Syst. Saf.*, vol. 216, 2021, Art. no. 107927.

[27] Q. Wang, S. Bu, Z. He, and Z. Y. Dong, "Toward the prediction level of situation awareness for electric power systems using CNN-LSTM network," *IEEE Trans. Ind. Informat.*, vol. 17, no. 10, pp. 6951–6961, Oct. 2021.

[28] X. Xu et al., "CARes-UNet: Content-aware residual UNet for lesion segmentation of COVID-19 from chest CT images," *Med. Phys.*, vol. 48, no. 11, pp. 7127–7140, 2021.

[29] T. O. Ayodele, "Types of machine learning algorithms," in *New Adv. Mach. Learn.*, vol. 3, 2010, pp. 19–48.